Supplementary information

High-flux nickel foam electrodes with asymmetric binder engineering for efficient electrolyte transport and CO_2 regeneration in reactive carbon capture

Youngjin Doh[1], Jaeyeon Lee[1], Junwon Oh, Yeomin Kang, Ki Tae Park*

Department of Chemical Engineering, Konkuk University, 120 Neungdong-ro, Gwangjin-gu, Seoul 05029, Republic of Korea

Corresponding authors

*E-mail addresses: kpark@konkuk.ac.kr (K.T. Park)

[1]These authors contributed equally to this work.

1. Experimental section

Materials

Nickel foam (eq-bcnf-16m, purity > 99.99%, porosity ≥ 95%) was purchased from MTI, and carbon paper (Sigracet 39BB) was used as received. Silver nanoparticles (Ag NPs, <100 nm) were obtained from Sigma-Aldrich, while acetylene black was purchased from Thermo Fisher Scientific. Ketjenblack (KB) was acquired from Sigma-Aldrich, and Vulcan XC-72 (VC) was obtained from Premetek. Teflon® (PTFE) dispersion (60 wt%) and cation-conducting ionomer (5 wt% Nafion solution) were purchased from Dupont. Sustainion XA-9 anion exchange ionomer (5% in ethanol) was supplied by Dioxide Materials, and bipolar membranes (Fumasep FBM) were obtained from Fumatech. Potassium bicarbonate ($KHCO_3$), potassium carbonate (K_2CO_3), and ethylenediaminetetraacetic acid (EDTA) were purchased from Sigma-Aldrich. A 1 M potassium hydroxide solution (KOH) was obtained from Samchun Chemicals. Isopropyl alcohol (IPA, 99.7%) and ethanol (99.5%) were purchased from J.T. Baker. All chemicals and materials were used as received from the manufacturers without any further purification.

Fabrication of electrodes

The nickel foam (NF) electrodes were fabricated via a sequential spray-coating method. First, the raw NF (geometric area of 2 cm × 2 cm) was pre-treated with a PTFE dispersion (5 wt%) to establish a basal hydrophobic framework. Subsequently, the micro porous layer (MPL) slurry, consisting of acetylene black and PTFE binder dispersed in isopropyl alcohol (IPA), was spray coated onto the pre-treated NF. The MPL coated NF was then sintered in a furnace at 350 °C for 1 h under N_2 atmosphere to thermally consolidate the PTFE binder. Finally, the catalyst layer (CL) slurry, comprising Ag nanoparticles and Nafion binder dispersed in IPA,

was ultrasonicated and spray-coated onto the MPL at 150 °C. The resulting asymmetric electrode was dried under ambient conditions to remove residual solvents.

For comparison, conventional carbon paper (CP) electrodes were prepared using an identical catalyst deposition method. A commercial CP substrate (39BB, SGL) (2 cm × 2 cm) with MPL was utilized directly without any hydrophobic pre-treatment or additional MPL coating. The identical CL slurry, comprising Ag nanoparticles and Nafion binder dispersed in IPA, was ultrasonicated and directly spray-coated onto the bare CP substrate at 150 °C. The resulting CP electrode was then dried under ambient conditions to ensure complete solvent removal.

Materials characterizations

Scanning electron microscopy (SEM) images of the sample were obtained using a field-emission scanning electron microscope (FE-SEM, SU5000, Hitachi, Japan) equipped with an energy-dispersive X-ray spectroscopy (EDS) detector (Ultim Max 40, Oxford Instruments, UK). X-ray diffraction (XRD) patterns of the catalyst layers before and after CO_2RR were obtained using an X-ray diffractometer (Smart Lab, Rigaku) with Cu Kα radiation (λ = 0.1542 nm). The intensity data were recorded in the 2θ range from 20 to 80 degrees at a scan rate of 5 °/min. The chemical states of the catalyst layers before and after CO_2RR were analyzed using an X-ray photoelectron spectrometer (XPS) (K-Alpha, Thermo Fisher Scientific) with Al radiation (1486.7 eV).

The mercury intrusion porosimetry (MIP) measurements were conducted using an AutoPore IV porosimeter (Micromeritics). The operating pressure range was set from 0.10 to 60,000 psia. For the pore size distribution calculations, the advancing contact angle of mercury was set to 130.0 degrees, and the surface tension of mercury was assumed to be 485 dynes/cm.

Electrochemical impedance spectroscopy (EIS) measurements of the GDEs were conducted in the MEA-type electrolyzer using a potentiostat/galvanostat (SP-300, BioLogic) in a frequency range from 200 kHz to 10 Hz, at a cell voltage of 3 V with an amplitude of 10 mV. Cyclic voltammetry (CV) was conducted within a narrow, non-Faradaic potential window of 100 mV (0.83 to 0.93 V vs. RHE for the NF electrode, and 0.70 to 0.80 V vs. RHE for the CP electrode). The measurements were performed at varying scan rates of 20, 40, 60, 80, 100, and 120 mV/s, in a 3 M $KHCO_3$ solution to calculate the electrochemically active surface area (ECSA) of the electrodes. For these experiments, an Ag/AgCl electrode served as the reference electrode, and all measured potentials were calibrated to the reversible hydrogen electrode (RHE) scale using the Nernst equation: E(RHE) = E(Ag/AgCl) + 0.197 + 0.059 × pH. The double-layer capacitance (C_{dl}) was determined from the linear slope of the capacitive current density (Δj) versus the scan rate.

Raman setup

Operando Raman spectra were acquired using a fiber-optic spectrometer (i-Raman Plus BWS465-532S, B&W Tek) equipped with a 532 nm excitation laser and a high quantum efficiency TE cooled CCD detector, providing a spectral resolution of 3.5 cm^{-1}. The laser was focused onto the catalyst-electrolyte interface through the backside of the macroporous Ni foam using a long working distance objective lens (Olympus LMPLanFL N, 20x). To avoid thermal degradation of the sample while maintaining an optimal signal to noise ratio, the incident laser power was regulated to 15 mW (50% of the maximum output). Each spectrum was collected over a wide wavenumber range (-55 to 3500 cm^{-1}) with an exposure time of 20 s and 5 accumulations. For the quantitative analysis of the local pH, the specific spectral window containing the bicarbonate and carbonate peaks was extracted. All raw spectral data

were subsequently processed using OriginPro software. The processing protocol included signal smoothing, baseline correction, and peak deconvolution to accurately determine the integrated areas of the target peaks.

Raman pH calculation

The local surface pH during the electrochemical CO_2 reduction was determined by analyzing the ratio of bicarbonate (HCO_3^-) and carbonate (CO_3^{2-}) species derived from their respective Raman signal areas (S). The Raman bands located at approximately 1017 and 1066 cm^{-1} were assigned to the vibrational modes of HCO_3^- and CO_3^{2-}, respectively.

Assuming that the total active carbon concentration is conserved at the electrode-electrolyte interface, the local concentrations of each species were calculated. Given the catholyte composition of 3.0 M $KHCO_3$ without additional chelating agents, the total effective inorganic carbon concentration was set to 3.0 M. The specific concentrations were quantified as follows:

$$c_{HCO_3^-} = 3.0 \times \frac{S_{HCO_3^-}}{S_{HCO_3^-} + S_{CO_3^{2-}}} \quad \text{(Eq. 1)}$$

$$c_{CO_3^{2-}} = 3.0 \times \frac{S_{CO_3^{2-}}}{S_{HCO_3^-} + S_{CO_3^{2-}}} \quad \text{(Eq. 2)}$$

To rigorously account for the high ionic strength (Im) of the concentrated electrolyte, the activity coefficients (y) of the ionic species were estimated using the extended Davies equation:

$$\log \gamma = -AZ_i^2\left(\frac{\sqrt{I_m}}{1+\sqrt{I_m}} - 0.2I_m\right) \quad \text{(Eq. 3)}$$

where Zi is the valence of the ion and A is a temperature-dependent constant. The surface pH was subsequently calculated based on the thermodynamic equilibrium of the HCO_3^-/ CO_3^{2-} system utilizing the proton activities (a_{H^+}). Finally, an empirical calibration correction factor (-0.22) was applied to the simulated values to offset the deviation caused by the extremely high ionic strength, yielding the final $pH_{surface}$.[1]

Surface pH analysis was conducted using OriginPro software to calculate the initial pH values (pH_{raman}) based on the relative peak intensities corresponding to HCO_3^- and CO_3^{2-}. For validation, standard solutions with varying $KHCO_3$ and K_2CO_3 ratios (c_{total} = 3 M) were prepared. The bulk pH of these solutions was measured via a standard pH meter and directly compared against the Raman-derived pH values (Table S4). Because the uncalibrated pH_{raman} was consistently higher than the actual measured bulk pH, a constant correction factor was applied. The final $pH_{surface}$ was modified by subtracting the experimental difference of 0.22, as expressed in Eq. 4:

$$pH_{surface} = pH_{raman} - 0.22 \quad \text{(Eq. 4)}$$

Table S1. The measured bulk pH and Raman-derived pH values (before and after modification) for different concentration ratios of HCO_3^- and CO_3^{2-} solutions. The total concentration c_{total} is 3 M.

$c(HCO_3^-)/c(CO_3^{2-})$	**Measured pH**	**pH_{raman} (before modification)**	**$pH_{surface}$ (after modification)**
85	8.66	8.87	8.66
25	9.11	9.32	9.11
5	9.63	9.83	9.61

1	10.41	10.65	10.43

Electrochemical CO_2 Reduction measurement

The direct electrochemical conversion of the bicarbonate solution was performed in a membrane electrode assembly (MEA) configuration incorporating a bipolar membrane (BPM). The MEA-BPM cell was assembled using serpentine flow plates, featuring a Pt mesh as the anode and the fabricated Ni foam-based electrode (or CP electrode) with a geometric active area of 4 cm^2 serving as the cathode. The anolyte (1 M KOH) and catholyte (3 M $KHCO_3$) were continuously circulated through their respective flow channels at a constant rate of 20 mL/min, driven by Eldex precision high-pressure metering pumps. A trace amount of EDTA was introduced into the catholyte to sequester adventitious heavy metal impurities that would otherwise promote HER at the cathode, ensuring that performance trends reflect electrode geometry rather than electrolyte contamination. Additionally, high-purity CO_2 gas (99.999%) was continuously introduced into the catholyte reservoir at a flow rate of 200 sccm, precisely regulated by a mass flow controller (MFC, Alicat Scientific).

The electrochemical performance was evaluated using a potentiostat (SP-300, Bio-Logic) operating in chronopotentiometry (CP) mode. The applied current densities were systematically stepped either from 25 to 200 mA/cm^2 (in 25 mA/cm^2 increments) or from 50 to 400 mA/cm^2 (in 50 mA/cm^2 increments). Each specific current density condition was maintained for 720 s.

The gaseous products emerging from the cathode outlet were continuously channeled into an online gas chromatograph (GC; 8890, Agilent) and analyzed throughout the entire 720 s

duration of each step. Within the GC system, H_2 was quantified using a thermal conductivity detector (TCD), while CO was detected using a flame ionization detector (FID) equipped with a methanizer. Concurrently, the total volumetric flow rate of the product gas stream was monitored using a mass flow meter (MFM, wizro) to allow for the accurate determination of product yields.

Product analysis and performance evaluation

The performance metrics of the CO_2 reduction reaction (CO_2RR) were evaluated based on the Faradaic efficiency (FE) and energy efficiency (EE) of the gaseous products. The number of moles for each product (n) was determined using the ideal gas law (PV = nRT). For this calculation, the total volume of the exit gas was measured using a mass flow meter (MFM). The reference temperature and pressure for the volume conversion were set to 293.15 K (20 °C) and 1 bar, respectively.

The Faradaic efficiency (FE) for each gas product was calculated using the following equation:

$$FE(\%) = \frac{z \times N \times F}{Q} \times 100 \quad \text{(Eq. 5)}$$

where z is the number of electrons transferred for the formation of the specific product (which is 2 for both CO and H_2), n is the number of moles of the product quantified by the gas chromatograph (GC) and MFM, F is the Faraday constant (96,485 C/mol), and Q is the total charge (C) passed during the reaction period.

The overall energy efficiency (EE) of the system was evaluated based on the higher heating value (HHV) of the generated syngas (CO and H_2) relative to the total electrical energy applied to the cell. The EE was calculated using the following equation:

$$EE(\%) = \frac{(n_{CO} \times HHV_{CO} + n_{H_2} \times HHV_{H_2})}{Q \times V_{cell}} \times 100 \quad \text{(Eq. 6)}$$

where HHV_{CO} and HHV_{H2} are the higher heating values of CO (284,580 J/mol) and H_2 (286,440 J/mol), respectively. V_{cell} represents the applied cell voltage (V) during the chronopotentiometry measurement, and Q represents the total applied charge (C).

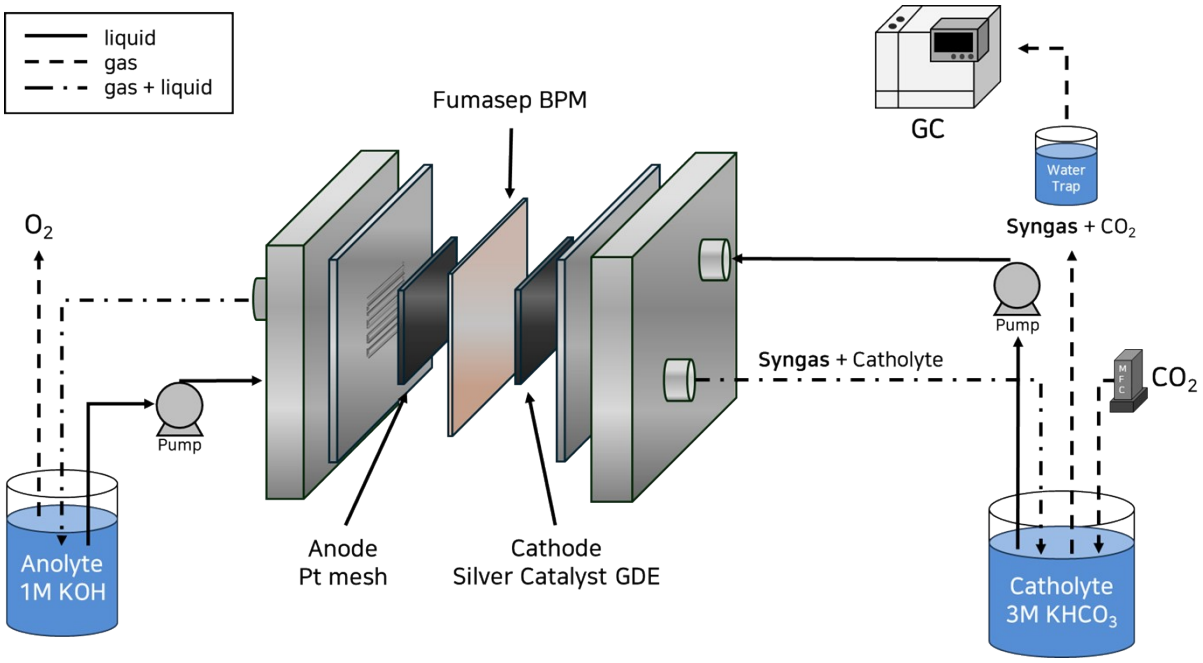

Figure S1. Schematic of the BPM-based MEA-type RCC systems. The diagram highlights the circulation of 1M KOH anolyte and 3M $KHCO_3$ catholyte, the CO_2 gas delivery system, and the online gas chromatography (GC) setup for real-time product analysis.

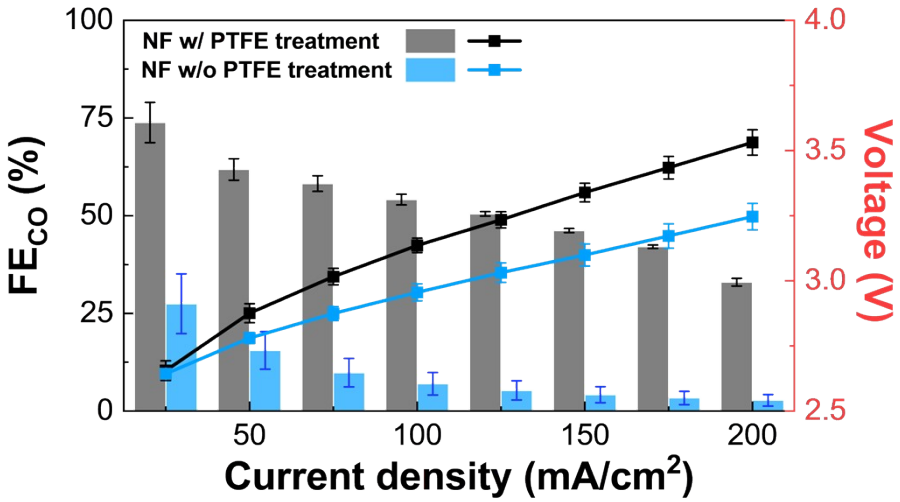

Figure S2. Electrochemical performance of the Ni foam-based electrode prepared without PTFE pre-treatment of the substrate (MPL loading: 1 mg/cm^2, CL loading: 3 mg/cm^2).

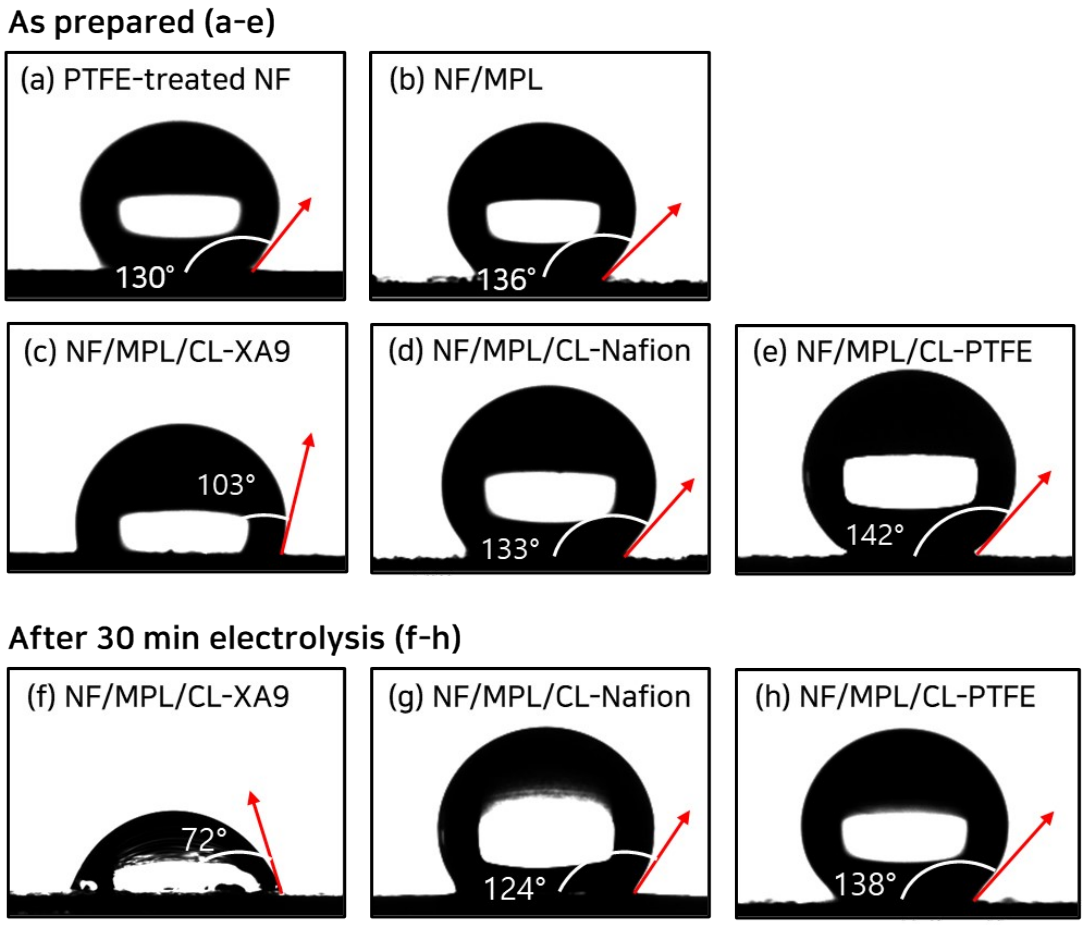

Figure S3. Water contact angle measurements of the electrodes. As-prepared: (a) PTFE-treated Ni foam (NF), (b) NF coated with a microporous layer (MPL), and Ag catalyst layers (CL) on NF/MPL using (c) XA-9, (d) Nafion, and (e) PTFE binders. After electrolysis: CLs using (f) XA-9, (g) Nafion, and (h) PTFE binders.

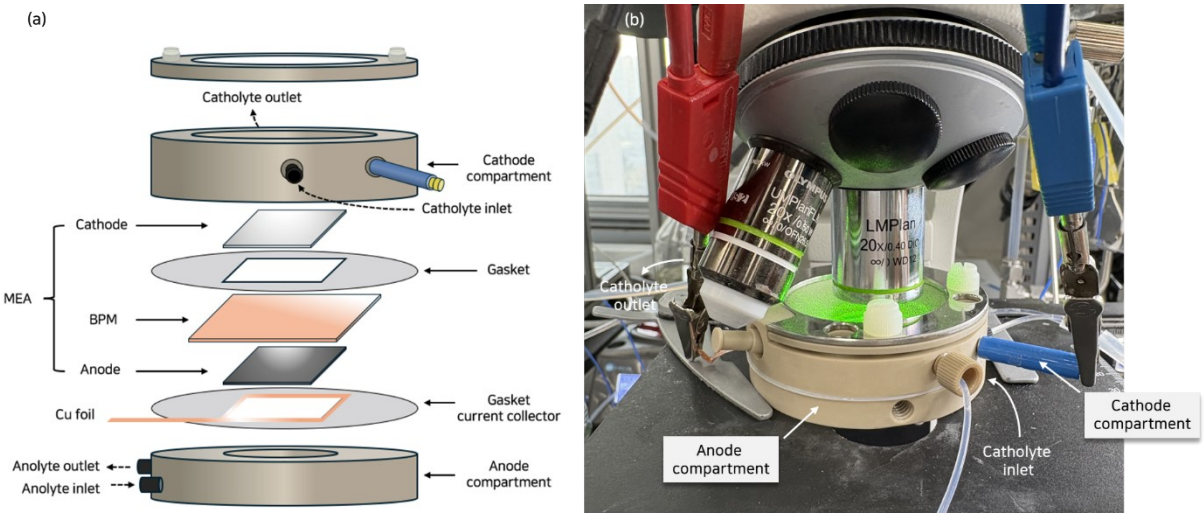

Figure S4. Configuration of the operando Raman spectroscopy setup. (a) Schematic illustration of the custom-designed Raman cell, constructed to mimic the actual membrane electrode assembly (MEA) environment. (b) Optical photograph of the experimental setup during the measurement.

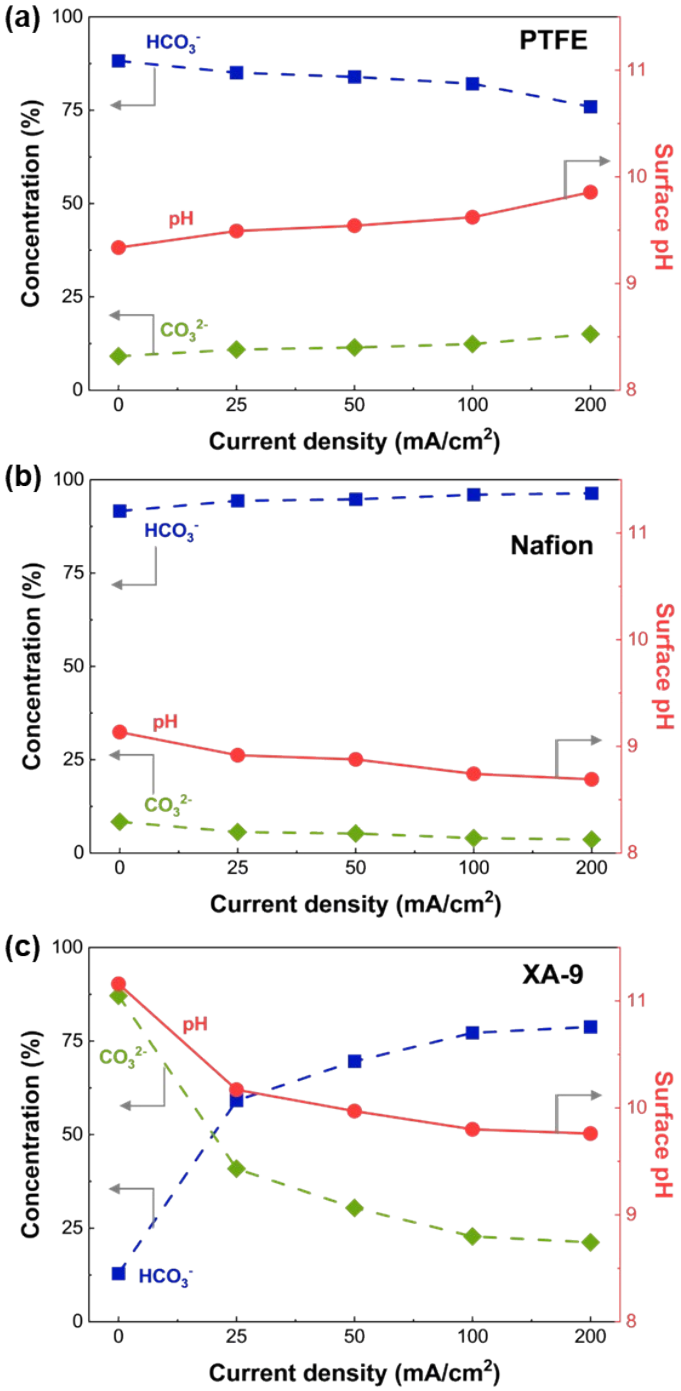

Figure S5. Quantitative evaluation of the surface speciation and local pH for different MPL binders. The relative concentrations (%) of HCO_3^- and CO_3^{2-} alongside the calculated interfacial pH are plotted as a function of applied current density for electrodes utilizing (a) PTFE, (b) Nafion, and (c) XA-9 binders in the MPL.

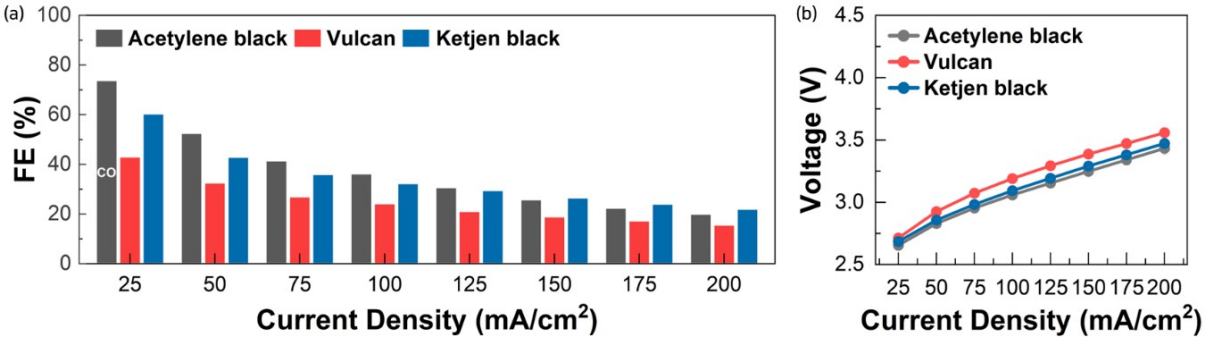

(c)

	Acetylene black	Vulcan	Ketjen black
Hydrophobicity	●	◎	○
Conductivity	●	◎	●
Specific Surface Area	○	◎	●
Structure/porosity	◎	◎	●

○: Low
◎: Medium
●: High

Figure S6. Electrochemical performance comparison of different carbon black supports. (a) FE_{CO} and (b) cell voltage versus applied current density. (c) Physical properties of the carbon blacks.

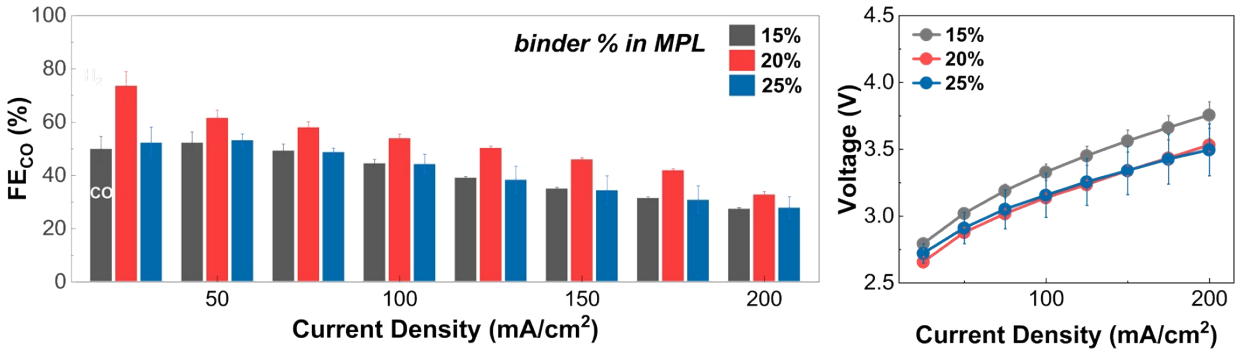

Figure S7. Electrochemical performance dependence on the PTFE binder concentration (15%, 20%, and 25%) in the MPL.

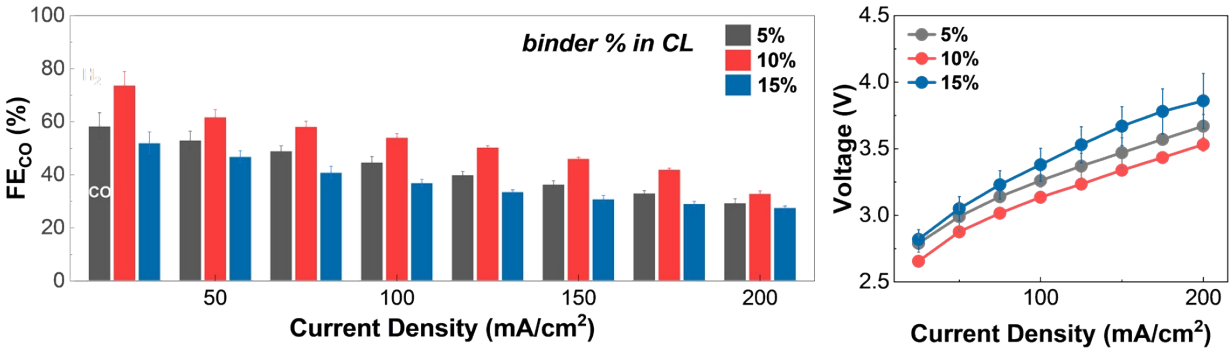

Figure S8. Electrochemical performance dependence on the Nafion binder concentration (5%, 10%, and 15%) in the CL.

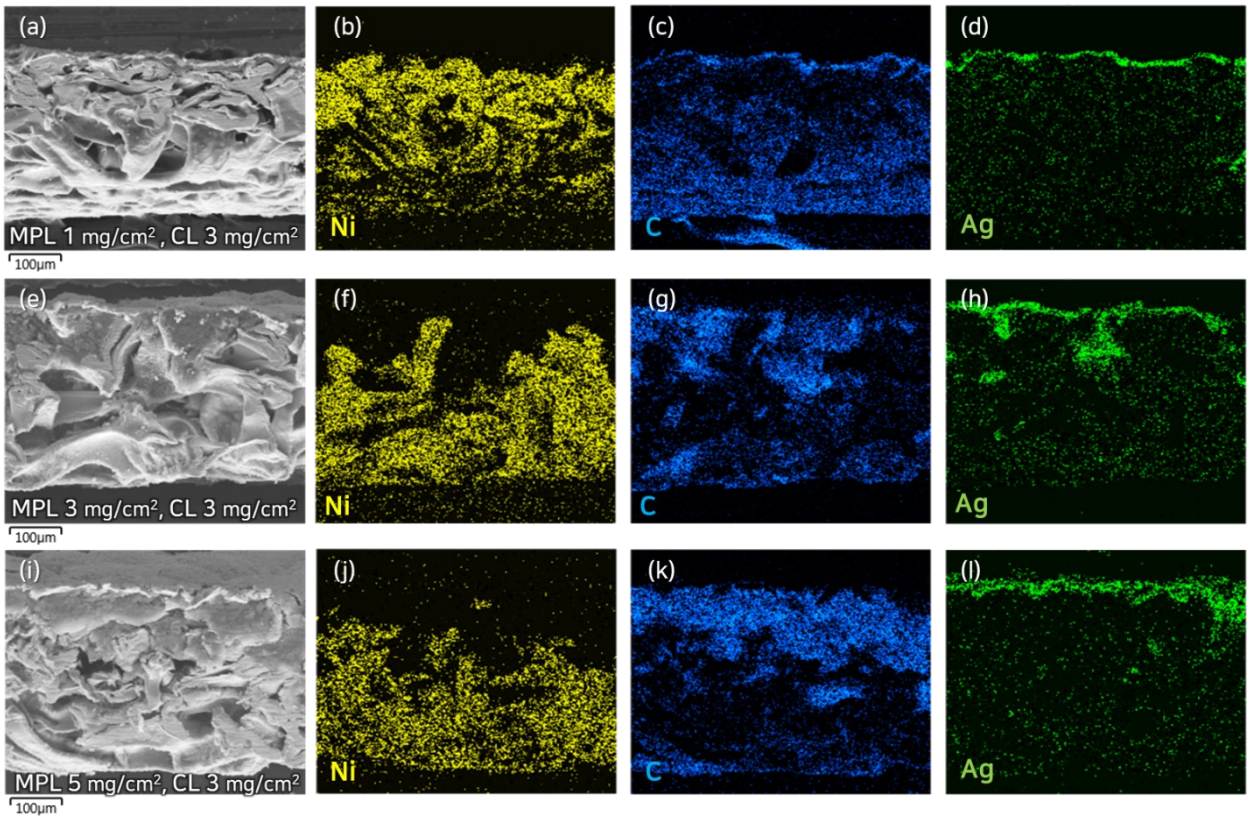

Figure S9. Cross-sectional morphology and compositional distribution of the electrodes. Cross-sectional SEM images and corresponding EDS elemental mapping for (a–d) 1 mg/cm², (e–h) 3 mg/cm², and (i–l) 5 mg/cm² MPL loadings with a CL loading of 3 mg/cm².

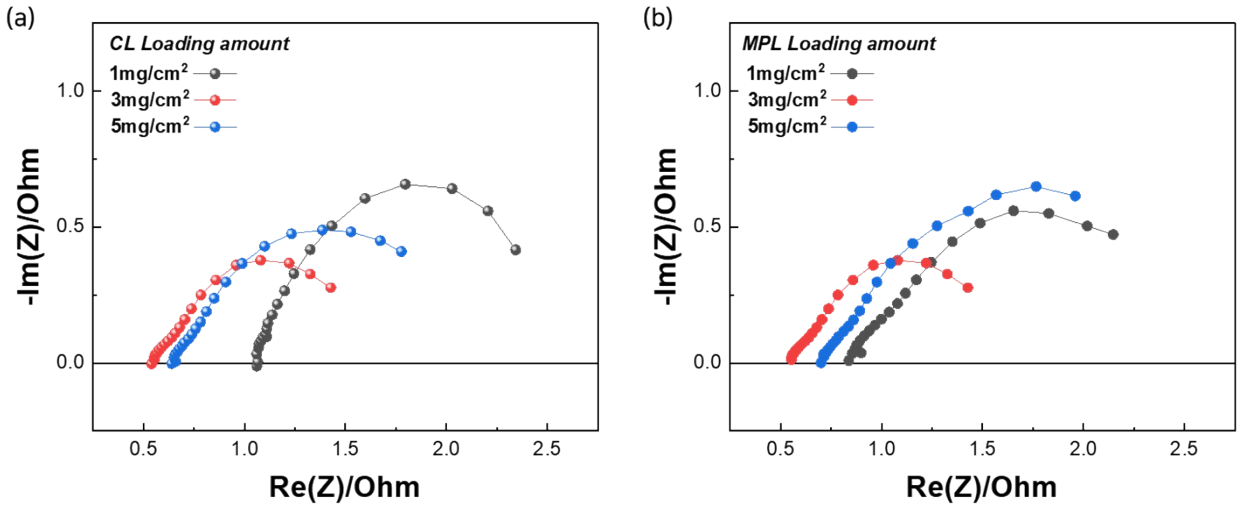

Figure S10. Electrochemical impedance spectroscopy (EIS) analysis for optimizing the electrode architecture. Nyquist plots are shown for electrodes with varying (a) micro-porous layer (MPL) loadings and (b) catalyst layer (CL) loadings.

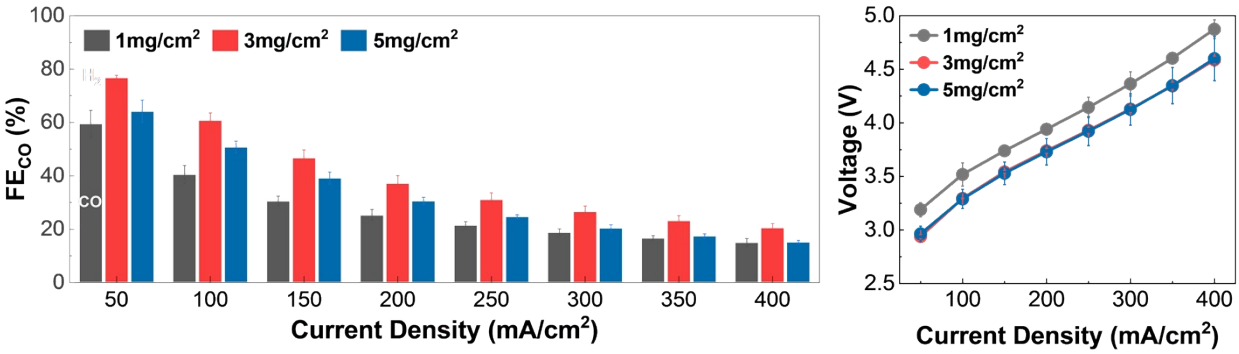

Figure S11. Optimization of the catalyst layer (CL) loading. (a) FE_{CO} and (b) cell voltage as a function of applied current density for different CL loadings (1, 3, and 5 mg/cm^2). The MPL loading was fixed at the optimized value of 3 mg/cm^2.

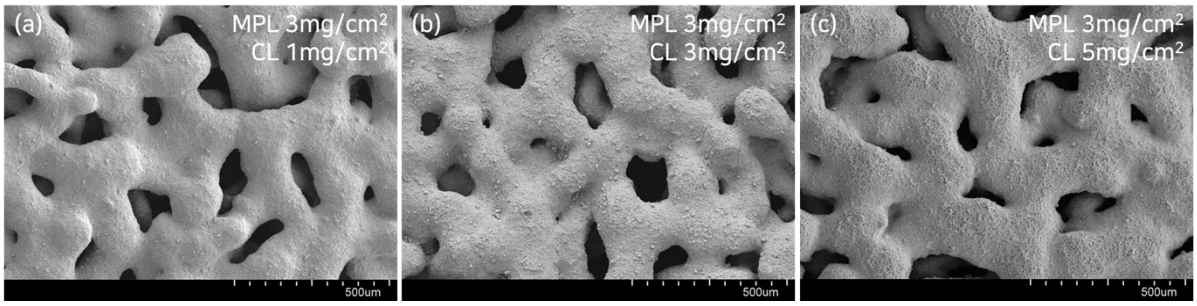

Figure S12. SEM images corresponding to Ag catalyst loadings of (a) 1, (b) 3, and (c) 5 mg/cm^2, respectively, with the fixed MPL loading of 3 mg/cm^2.

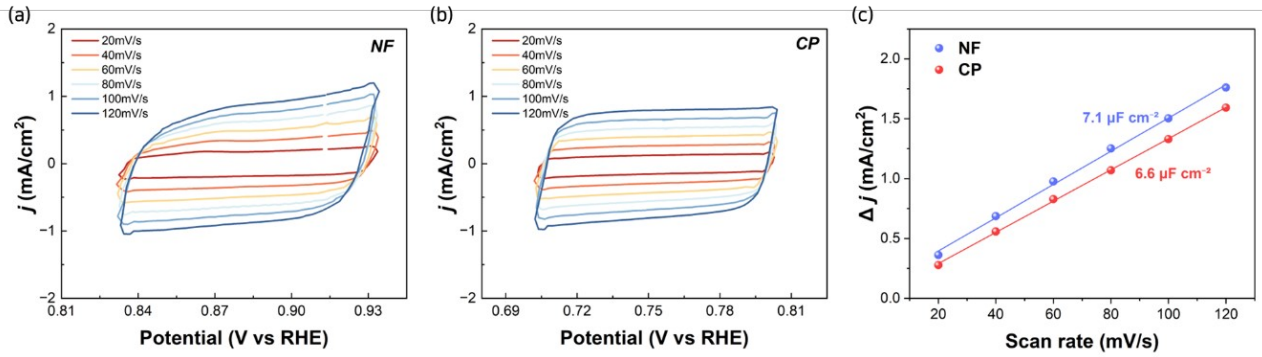

Figure S13. Determination of electrochemically active surface area (ECSA) via double-layer capacitance (C_{dl}) measurements. (a, b) CV curves recorded at various scan rates (20–120 mV/s) in the non-Faradaic region for (a) NF and (b) CP electrodes. (c) Linear fitting of the capacitive current density as a function of scan rate. The derived C_{dl} values are 7.1 μF cm^{-2} for NF and 6.6 μF cm^{-2} for CP, respectively.

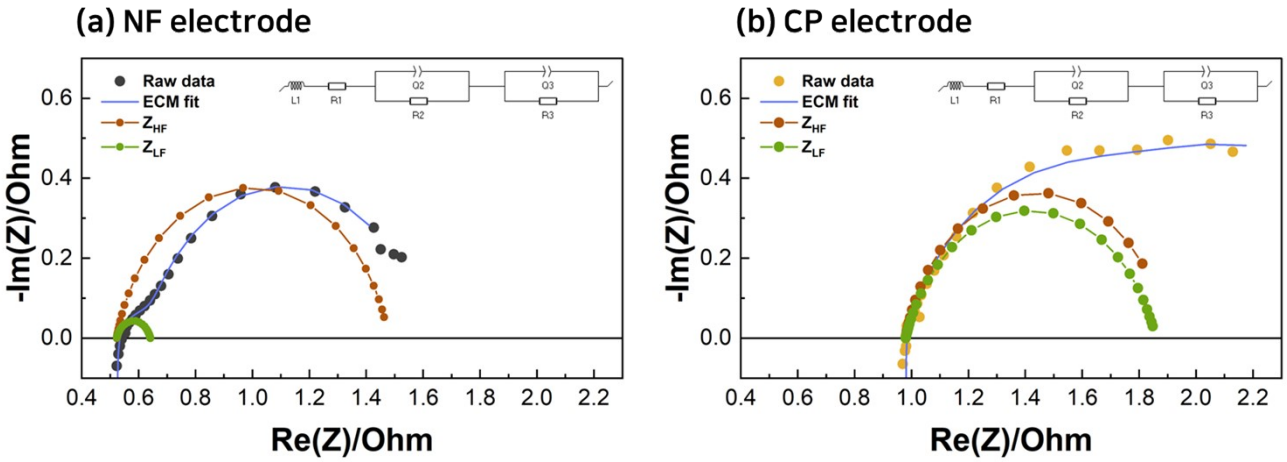

Figure S14. EIS analysis and equivalent circuit fitting (L_1 + R_1 + Q_2/R_2 + Q_3/R_3) for (a) the optimized NF and (b) conventional CP electrodes. The deconvoluted spectra separate the high-frequency charge transfer (Z_{HF}, brown) and low-frequency mass transport (Z_{LF}, green) impedances.

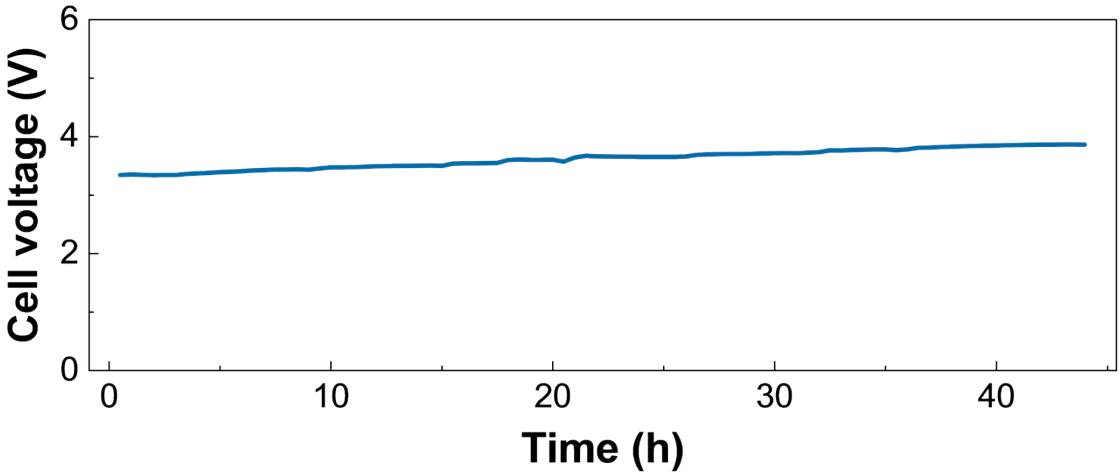

Figure S15. Extended cell voltage stability profile of the optimized NF electrode. The plot shows the cell voltage during a 44 h chronopotentiometry test at a constant current density of 100 mA/cm^2.

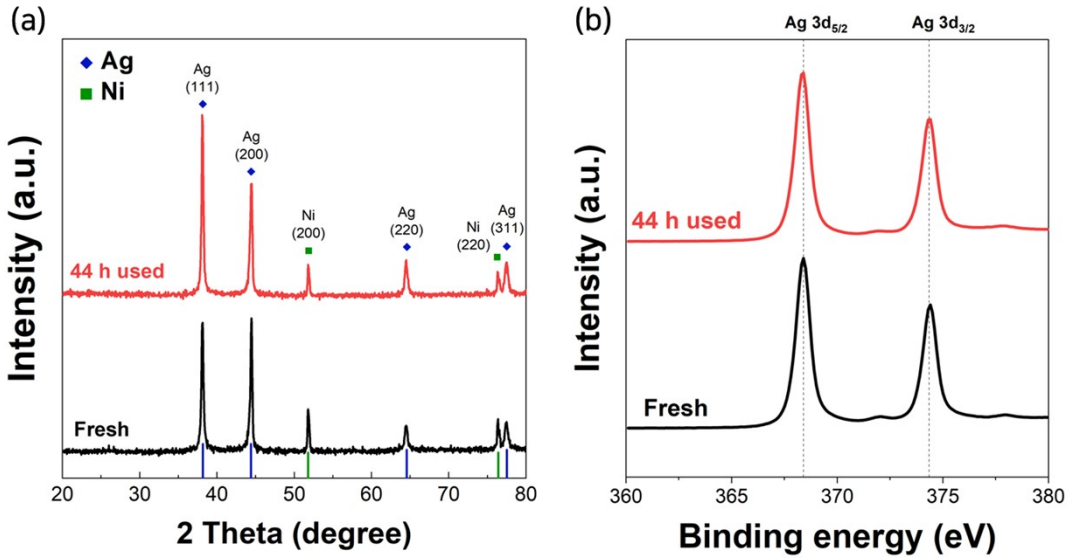

Figure S16. Evaluation of the long-term stability of the Ag electrode. (a) XRD patterns of the fresh and 44 h used electrodes. (b) High-resolution Ag 3d XPS spectra before and after 44 h of electrolysis.

Table S2. Comparison of electrochemical CO_2 reduction performance between the optimized Ni foam-based Ag electrode and other reported electrocatalysts.

Cathode	Electrolyte	Reactor	j_{total} (mA/cm²)	FE_{CO} (%)	|Cell Voltage| (V)	Ref.
Ni foam-based Ag electrode	3 M $KHCO_3$	BPM-MEA	100	62.6	3.26	this work
			200	41	3.71	
			300	30.1	4.10	
			400	23.2	4.56	
Ni-SAC	3 M $KHCO_3$	BPM-MEA	100	97	3.26	2
			200	94	3.7	
Ag/GDL	3 M $KHCO_3$	BPM-MEA	100	37	3.5	3
Freestanding porous Ag	3 M $KHCO_3$	BPM-MEA	100	59	3.6	4
			200	34	4.4	
Ag foam	3 M $KHCO_3$	BPM-MEA	100	59	4	5
Electrodeposited Ag	3 M $KHCO_3$	BPM-MEA	100	65	3.65	6
			200	41	4.5	
Ag	1 M K_2CO_3	BPM-MEA	100	28	3.3	7
			200	20	3.7	
Ag electrode	Carbonate electrolyte	CEM-MEA	100	43	3.4	8
			200	46	3.8	
AgC	3 M $KHCO_3$	BPM-MEA	100	68	3.6	9
Ag-C-AEI	3 M $KHCO_3$	CEM-MEA	100	57	3.17	10
			200	44	3.36	
AgC	$KHCO_3$	BPM-MEA	100	71	4.6	11
Ni-N/C	2M K-GLY with 0.1M KH_2PO_4	CEM-MEA	100	45	3.5	12
			200	37	4.1	

Reference

1. Z. Zhang, L. Melo, R. P. Jansonius, F. Habibzadeh, E. R. Grant and C. P. Berlinguette, *ACS Energy Lett.*, 2020, **5**, 3101-3107.
2. H. Song, C. A. Fernández, H. Choi, P.-W. Huang, J. Oh and M. C. Hatzell, *Energy Environ. Sci.*, 2024, **17**, 3570-3579.
3. T. Li, E. W. Lees, M. Goldman, D. A. Salvatore, D. M. Weekes and C. P. Berlinguette, *Joule*, 2019, **3**, 1487-1497.
4. Z. Zhang, E. W. Lees, F. Habibzadeh, D. A. Salvatore, S. Ren, G. L. Simpson, D. G. Wheeler, A. Liu and C. P. Berlinguette, *Energy Environ. Sci.*, 2022, **15**, 705-713.
5. Z. Zhang, E. W. Lees, S. Ren, B. A. W. Mowbray, A. Huang and C. P. Berlinguette, *ACS Cent. Sci.*, 2022, **8**, 749-755.
6. E. W. Lees, M. Goldman, A. G. Fink, D. J. Dvorak, D. A. Salvatore, Z. Zhang, N. W. X. Loo and C. P. Berlinguette, *ACS Energy Lett.*, 2020, **5**, 2165-2173.
7. Y. C. Li, G. Lee, T. Yuan, Y. Wang, D.-H. Nam, Z. Wang, F. P. García de Arquer, Y. Lum, C.-T. Dinh, O. Voznyy and E. H. Sargent, *ACS Energy Lett.*, 2019, **4**, 1427-1431.
8. Y. C. Xiao, C. M. Gabardo, S. Liu, G. Lee, Y. Zhao, C. P. O'Brien, R. K. Miao, Y. Xu, J. P. Edwards, M. Fan, J. E. Huang, J. Li, P. Papangelakis, T. Alkayyali, A. Sedighian Rasouli, J. Zhang, E. H. Sargent and D. Sinton, *EES Catal.*, 2023, **1**, 54-61.
9. Y. Kim, E. W. Lees and C. P. Berlinguette, *ACS Energy Lett.*, 2022, **7**, 2382-2387.
10. S. I. Suh, Y. Lee, J.-y. Choi, H. Kim, H.-S. Oh and W. H. Lee, *J. Energy Chem.*, 2025, **110**, 427-433.
11. R. Ahmadi, S. E. Dillon, A. M. L. Jewlal, Y. Kim, M. Namdari and C. P. Berlinguette, ACS Energy Lett., 2025, **11**, 473-480.
12. Y. C. Xiao, S. S. Sun, Y. Zhao, R. K. Miao, M. Fan, G. Lee, Y. Chen, C. M. Gabardo, Y. Yu, C. Qiu, Z. Guo, X. Wang, P. Papangelakis, J. E. Huang, F. Li, C. P. O'Brien, J. Kim, K. Han, P. J. Corbett, J. Y. Howe, E. H. Sargent and D. Sinton, *Nat. Commun.*, 2024, **15**, 7849.